Transport in Porous Media (2006) 65: 443–467
DOI 10.1007/s11242-006-0006-z
© Springer 2006

reference [6]

3D Stochastic Modelling of Heterogeneous Porous Media – Applications to Reservoir Rocks

KEJIAN WU[1,*], MARINUS I.J. VAN DIJKE[1], GARY D. COUPLES[1], ZEYUN JIANG[1], JINGSHENG MA[1], KENNETH S. SORBIE[1], JOHN CRAWFORD[2], IAIN YOUNG[2] and XIAOXIAN ZHANG[2]
[1]*Institute of Petroleum Engineering, Heriot-Watt University, Edinburgh UK*
[2]*SIMBIOS, University of Abertay, Dundee*

(Received: 21 March 2005; in final form: 7 January 2006)

Abstract. The creation of a 3D pore-scale model of a porous medium is often an essential step in quantitatively characterising the medium and predicting its transport properties. Here we describe a new stochastic pore space reconstruction approach that uses thin section images as its main input. The approach involves using a third-order Markov mesh where we introduce a new algorithm that creates the reconstruction in a single scan, thus overcoming the computational issues normally associated with Markov chain methods. The technique is capable of generating realistic pore architecture models (PAMs), and examples are presented for a range of fairly homogenous rock samples as well as for one heterogeneous soil sample. We then apply a Lattice–Boltzmann (LB) scheme to calculate the permeabilities of the PAMs, which in all cases closely match the measured values of the original samples. We also develop a set of software methods – referred to as pore analysis tools (PATs) – to quantitatively analyse the reconstructed pore systems. These tools reveal the pore connectivity and pore size distribution, from which we can simulate the mercury injection process, which in turn reproduces the measured curves very closely. Analysis of the topological descriptors reveals that a connectivity function based on the specific Euler number may serve as a simple predictor of the threshold pressure for geo-materials.

Key words: 3D Markov random field, Markov chain Monte Carlo, pore space reconstruction, Lattice–Boltzmann method, specific Euler number, Percolation.

1. Introduction

Quantitative characterisation of porous media at the pore scale is of fundamental importance in many scientific subjects, including: composite materials (Dullien, 1992, Laakkonen, 2003), rheology (Müller and Saez, 1999), geophysics (Berryman and Wang, 2000), polymer flow through rock cores (Sorbie *et al.*, 1987), statistical physics (Hilfer, 2000), chemical physics

*Author for Correspondence: Tel.: +44-(0)-131-451-8299; Fax: +44-(0)-131-451-3127; e-mail: kejian.wu@pet.hw.ac.uk

(Spöler and Klapp, 2004), colloid science (Quiblier, 1984), petroleum engineering (Kantzas *et al.*, 1988), soil science (Crawford *et al.*, 1995, Young *et al.*, 2001) and biotechnology (Wanner *et al.*, 1995). A compelling motivation for such studies concerns the understanding, and eventually the prediction, of the single and multiphase transport properties of the medium. Within the subsurface, fluid flow through porous rocks is of major economic interest e.g. for the extraction of hydrocarbons, the exploitation of water supplies, the disposal of nuclear wastes, etc. This paper describes a new approach to make predictions of the transport characteristics of porous media by reconstructing the pore space numerically from thin sections. Examples are presented for a range of rock types that span much of the variability known for subsurface materials.

Mainstream research aimed at characterising porous media tends to involve three major steps as follows: (i) Obtaining a representative microstructure for the sample of interest (i.e. the reconstruction step); (ii) A quantitative characterisation of the microstructure which has been derived; (iii) Exact or approximate solutions of the equations of motion that govern the transport phenomenon of interest within the pore space construction. Steps (i) and (ii) may be almost inseparable, since some methods are based on tomographic imaging approaches. There are various ways to predict fluid flow properties based on solving the Navier–Stokes equations, e.g. using finite difference, finite element or Lattice–Boltzmann (LB) methods.

Previous attempts to quantitatively characterise the microstructure include methods which analyse the tortuosity and heterogeneity of the pore system. Typically, these approaches adopt the conventional paradigm of "pore bodies" linked by smaller connections or "pore throats". These analyses can be based on determining the probability of pore interconnection (Marshall, 1958), on pore shape (Currie, 1961), or on variation in pore diameter (Ball, 1981). Local porosity and percolation theories have been applied to homogeneous sandstones (Biswal *et al.*, 1998) to measure the geometric features of porous media and to determine the effective transport parameters.

In realistic porous media, fluid flow at the pore scale occurs within a complex three-dimensional (3D) network of pores. Typically, the pore network is an interconnected three-dimensional array of void spaces (e.g. in rocks, inter-granular porosity, fracture apertures, moldic porosity, etc) that can be characterised by geometrical quantities (pore size or volume, pore shape) and topological descriptors (pore connectivity). Progress in studying transport through heterogeneous porous media has been hampered by the difficulties involved in characterizing the complex microstructure of the pore system of real materials. There is a lack of effective and efficient methods to generate models of the complex microstructures, due to difficulties in analysing the precise geometry and topology of the pore system.

Existing reconstruction approaches can be grouped into those that seek to obtain direct images of the medium (Dunsmoir *et al.*, 1991; Coles *et al.*, 1994), and those that are based on creating a model of the medium, for example via some sort of stochastic process. Although direct measurements of a 3D microstructure are now available via synchrotron X-ray computed microtomography (Dunsmoir *et al.*, 1991; Coles *et al.*, 1994, 1996; Spanne *et al.*, 1994; Hazlett, 1995; Coker *et al.*, 1996), it is often difficult and expensive to obtain reliable "images" of the 3D pore structure. Such methods are also limited in terms of their scale of resolution, and there is a trade-off between resolution and sample size, which in turn relates to sample representativity.

In practice, information about the microstructure of porous materials is often limited to two-dimensional thin section images. Several techniques have been proposed to statistically generate 3D pore structures from spatial information derived from such 2D images (Joshi, 1974; Quiblier, 1984; Adler *et al.*, 1990, 1992; Roberts, 1997; Hazlett, 1997; Yeong and Torquato, 1998a,b; Manswart and Hilfer, 1998; Okabe and Blunt, 2004). These methods consist of measuring statistical properties, such as porosity, correlation and lineal path functions, on 2D thin section images of the sample. Random 3D models are then generated in such a manner that they match the measured statistical properties, such as two-point correlation functions. Recent quantitative comparisons of these models with tomographic images of sedimentary rocks have shown that statistical reconstructions may differ significantly from the original sample in their geometric connectivity (Hazlett, 1997; Biswal *et al.*, 1999; Manswart *et al.*, 2000; Øren and Bakke, 2003).

In a different approach to the stochastic generation of 3D pore structures, Bakke and Øren (1997) have developed a process-based reconstruction procedure which directly models the particle sedimentation process. This approach incorporates grain size distribution and other petrographical data obtained from 2D thin sections to reconstruct 3D sandstones. Øren and Bakke (2002) applied their procedure to reconstruct Fontainebleau sandstone, but this method involves intensive computing.

Another approach is to ignore the detailed structure of the porous medium and simply to represent the microstructure by an interconnected network based on the assumption that larger pores (pore bodies) are connected by smaller pores (throats) (Fatt, 1956; Kantzas *et al.*, 1988; Øren and Pinczewski, 1992; McDougall and Sorbie, 1995; Blunt *et al.*, 1995; Keller *et al.*, 1997; Øren *et al.*, 1994; Pereira *et al.*, 1996; Mani and Mohanty, 1998; van Dijke and Sorbie 2002). Within such network models, it is possible to define a distribution of pores and throats so that the model reproduces various aspects of two- and three-phase flow behaviour. Network models have quite successfully reproduced and explained a number of

experimental observations in two-phase (McDougall and Sorbie, 1995) and three-phase systems (van Dijke *et al.*, 2004) based on the relevant pore-scale physics. However, they have had limited success in a priori predicting the transport properties of realistic porous media.

Typically, most network models assume that the pore structure is random and that the various pore elements (i.e. the bonds or bonds + nodes) have an idealized geometry. There have been few attempts to construct pore networks that replicate the true detailed microstructure of the porous medium. In those cases, the simulations using stochastic networks provided a poor representation of the results from the direct network replica (Manswart *et al.*, 2000; Øren and Bakke, 2003). To date, there is no direct and unique link between images of the porous medium and the creation of suitable networks.

In summary, the existing microstructure models are either not very good or highly simplified representations of rock samples or they involve intensive computations to quantify even relatively homogeneous sandstone structures. Even the latter method encounters difficulties in representing the morphology of real materials. Therefore, a new method is needed to represent a wide range of heterogeneous porous media, in a relatively cheap way, which will allow us to gain improved understanding of flow processes in these media.

This paper outlines a new reconstruction method that belongs to the class of stochastic pore space modelling. The new method creates reconstructions of a heterogeneous (possibly) porous medium using Markov Chain Monte Carlo (MCMC) simulation. It considers spatial structure information (derived from 2D or 3D sample data – specifically, thin section data in the x, y and z planes) that identifies all the transition probabilities between the voids and solids of the medium for a given local training lattice stencil. The input data is taken from image analysis, but our approach differs in one very important respect from published two-point (or multi-point) correlation methods (e.g. Okabe and Blunt, 2004). The method that we have developed involves a complicated multiple-voxel interaction scheme (a high-order neighborhood system) to generate individual realisations that have structure characteristics matching the input data. This MCMC reconstruction approach and the models it generates are referred to as "pore architecture models", or PAMs.

In addition to the reconstruction method to produce the PAMs, we have also developed a set of tools – referred to as "pore analysis tools" or PATs – to quantitatively analyse the geometry and topology of the pore system of the reconstructed material. The reconstructed pore scale models (PAMs) are used as direct input flow simulations, which allows us to compute transport properties, such as permeability (using a Lattice–Botlzmann method) and mercury invasion capillary pressure curves (using an invasion

percolation algorithm). This represents a step towards the validation of our approach. Work which is currently underway will link the derived pore network systems (PAMs) to network modelling approaches that can derive higher-order and more difficult to predict, properties, such as multi-phase flow characteristics.

2. Model Development

2.1. BACKGROUND – MARKOV RANDOM FIELDS

The method proposed in this paper originates from image processing research, where Markov Random Fields (MRFs) are widely used (Geman and Geman, 1984). MRF theory is based on using only a small number of *local* conditions to predict global features based on given images. In other words, it considers the interaction (or dependence) of a few local neighbours, and some other geometrical descriptors, to generalise the overall morphological features of the image, which in this case is the porous medium. In typical usage, the image is pixelated, and the probability of each pixel being in a particular state (black or white, for example) is determined (or conditioned) by means of a transition matrix of conditional probabilities that is determined from the training (prior) image. (The phrases "dependence", "conditioned" and "prior" are the formal terms used in stochastic analysis).

One of the problems usually associated with MRFs (Geman and Geman, 1984) is, as for all conventional Markov Chain algorithms treat each pixel individually at each stage, that they are essentially iterative and involve intensive computations, particularly in 3D. However, there is a class of MRFs, called Markov Mesh Random Fields (MMRF), in which only a single-pass simulation is required. In contrast, the scanning algorithm updated the image a line (row or column) of pixels at a time. Convergence was much faster, theoretically, and typical simulated samples were visually more appealing (Qian and Titerington, 1991a). That approach was used previously to develop a method for reconstructing 2D thin section images (Wu *et al.*, 2004), and is the basis for the 3D algorithms described here. Extension of the Markov chain model from 2D to 3D is crucial, particularly because interframe, as well as intraframe, associations must be modelled.

If 3D information is available to "image" the medium (e.g. a 3D tomographic scan), it is possible to extract the geometry of the pore system using one of several methods (e.g. Øren *et al.*, 1998; Liang *et al.*, 2000; Silin *et al.*, 2003; Lindquist *et al.*, 2000). The new approach described here is also applicable in those cases. However, as mentioned above, 3D images are not always reliable in that they are expensive to acquire; and there

are limits in terms of size/resolution. On the other hand, 2D thin section images are cheap and easy to obtain from rock samples e.g. collected from outcrops, off-cuts from core plugs and even from drill cuttings. In addition, it is possible – using simple optical techniques – to identify the components of the medium (minerals comprising the grains, clay and microbial distribution, etc). Direct imaging techniques such as X-ray tomography do not accomplish this task. Confocal microscopy techniques could, in principle, identify the mineral components of the grains, but we are not aware of this being done in the context of reconstructing a porous rock.

In recent years, there have been many attempts to develop effective procedures for reconstructing 3D porous media from 2D thin section images (Quiblier, 1984; Adler *et al.*, 1990; Roberts, 1997). Our approach is also based on the use of thin section images (or equivalent SEM scans, or other data arrays that depict geometric patterns), and can take advantage of the identification of the separate components (e.g. clays).

Developments in stereology have helped the whole research community to appreciate that a 2D image is not completely representative of the 3D medium. However, our method uses 2D information from three perpendicular cross-sections (ideally), which implicitly sample the topological characteristics of the 3D medium, to build our 3D models. Based on this idea, we have developed a new method to generate model structures that have topological properties that are similar to the original sample (as revealed in the thin sections). To be more specific, we use the set of three perpendicular images, obtained from a single rock sample, as a prior that determines the transition probabilities controlling the Markov Chain process that we describe more fully below.

The remainder of this section of the paper consists of four sub-parts. The model development is described first, where we outline the concepts underlying Markov Mesh models, and specify the assumptions. In the next part, the new scanning algorithm is described, and the MCMC method is explained. Then descriptions of a selection of rock models created using the approach are presented. Finally, we introduce some results obtained using those models as input to flow simulations. These flow results represent a preliminary validation of the model since a comparison of simulated permeability and laboratory-derived values are very close.

2.2. 3D MARKOV CHAIN MODEL

To describe the probability distribution function (PDF) that is used for characterising the microstructure (i.e. the texture) of the medium, we use the following notation. Suppose we have a finite array (lattice) of n voxels, the sample space, that are labelled by integers $i = 1, \ldots, n$. Let $X = (X_1, \ldots, X_n)$ be the "state/colour" of the voxels, where X_i represents the

event that site i has a given state x_i, i.e. 0 or 1 for pore or solid respectively, in a binary system. Strictly, to reconstruct a 3D porous medium we need the full PDF $p(x)$ for X, for which it is required to draw a perfect random sample from the sample space. However, this is impracticable, because the 3D sample space is too large for a normalizing constant to be calculated directly, so instead of deriving a PDF, we have adopted Markov Random Field models by assuming that the state of any site depends on the states of only a small number of neighbouring sites. To be more specific, for a particular site s, let Λ_{-s} denote set of all sites other than s. Then there exists a neighbourhood of s, $\mathcal{N}_s$, such that

$$p(x_s|x(\Lambda_{-s})) \approx p(x_s|x(\mathcal{N}_s)) \tag{1}$$

A MRF can be thought of as the multi-dimensional version of a Markov Chain. In other words, MRF formulations adopt a conditional probability perspective in a discrete stochastic process whose global properties are controlled by local characteristics. In general, distributions such as (1) are difficult to simulate, and existing iteration methods take a long time to reach convergence, thus limiting the application in practice, particularly in high-dimensional cases. However, for the 2D case, a new single-pass simulation has been developed to find the conditional probabilities (Qian and Titerington, 1991a; Wu *et al.*, 2004). In this paper, we consider the 3D case, which is a direct analogue of the 2D approach. In 3D, instead of pixels, the sites are voxels.

To build a 3D Markov Chain model for a lattice of voxels, we need the following notations. Let $V_{LMN} = \{(l, m, n) : 0 < l \leqslant L$ rows, $0 < m \leqslant M$ columns, $0 < n \leqslant N$ layers$\}$ be a finite integer lattice and let $(i,\ j,\ k)$ be a voxel at the intersection of row i, column j, and layer k, with associated state X_{ijk}. V_{ijk} denotes the rectangular parallelepiped array of voxels depicted in Figure 1 with associated state vector $X(V_{ijk})$. Since a single-pass scanning scheme will be used in our algorithm, instead of an intensive iteration method, we have to define the "past" voxels of $(a,\ b,\ c)$ which is the set $\{(l, m, n) : l < a$ or $m < b$ or $n < c)\}$. The past voxels depend on the chain direction. For example, if we run the chain from the bottom upwards (along the z direction) layer after layer, then all the voxels in the lower layers, i.e. $n < k$, will be the past voxels. At the current layer, if the chain is run from inside to outside (along the x direction) and from left to right (along the y direction), the past voxels will be $l < i$ and $m < j$. In general the chain can be run in any direction.

The Markovian assumption for this third order model is that

$$p(x_{ijk}|\{x_{lmn} : l < i \text{ or } m < j \text{ or } n < k\}) = p(x_{ijk}|x_{i-1,j,k}, x_{i,j-1,k}, x_{i,j,k-1}) \tag{2}$$

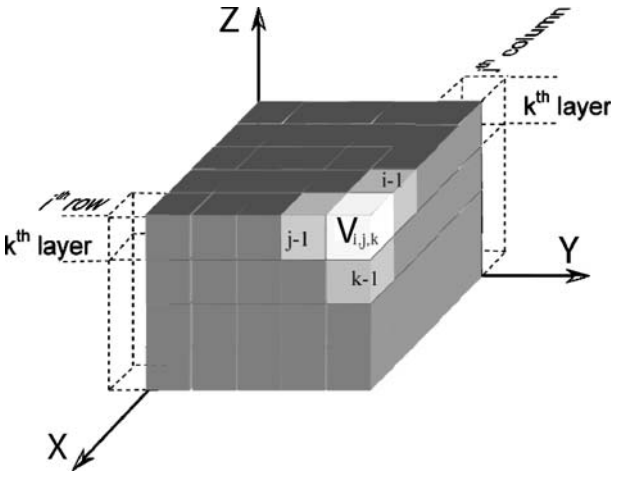

Figure 1. Definition of V_{ijk} in the 3D Markov chain model.

Then, for any $(i, j, k) \in V_{LMN}$, we have the joint probability function

$$p(x(V_{ijk})) = \prod_{l=0}^{i} \prod_{m=0}^{j} \prod_{n=0}^{k} p(x_{lmn} | x_{l-1,mn}, x_{l,m-1,n}, x_{lm,n-1}) \tag{3}$$

with lower order conditioning if any of the labels equals 0 (Qian and Titerrington, 1991b).

According to equation (1) a general MRF for a lattice would use the conditional probabilities

$$p(x_{ijk} | \{x_{lmn} : (l, m, n) \neq (i, j, k)\}) = p(x_{ijk} | \{x_{lmn} : (l, m, n) \in \mathcal{N}(ijk)\}) \tag{4}$$

where $\mathcal{N}(ijk)$ is a neighbourhood of (i, j, k). For example, for the 19-neighbourhood with the nearest 18 neighbours would be

$$\mathcal{N}_{19}(ijk) = \begin{bmatrix} (i-1, j, k) & (i, j-1, k) & (i, j, k-1) \\ (i+1, j, k) & (i, j+1, k) & (i, j, k+1) \\ (i, j-1, k+1) & (i-1, j, k+1) & (i-1, j+1, k) \\ (i, j+1, k-1) & (i+1, j, k-1) & (i+1, j-1, k) \\ (i, j+1, k+1) & (i+1, j, k+1) & (i+1, j+1, k) \\ (i, j-1, k-1) & (i-1, j, k-1) & (i-1, j-1, k) \end{bmatrix} \tag{5}$$

as shown in Figure 2a. Notice that this neighbourhood also includes "future" voxels and the associated MRF would need an iterative method. In contrast, to set up our MMRF we use a neighbourhood involving past voxels only. To make the chain run more efficiently, we use an algorithm generating two voxels simultaneously, voxel (i, j, k) and the right voxel $(i, j+1, k)$, similar to the 2D scanning algorithm introduced by Wu *et al.*,

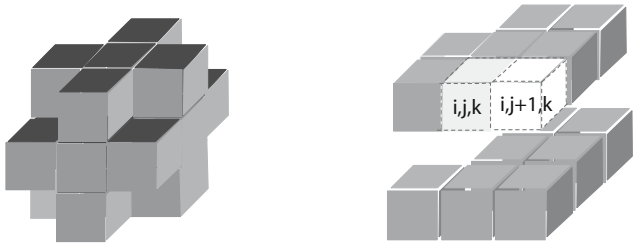

Figure 2. 19-neighbourhood and 15-neighbourhood systems in 3D, corresponding to equations (5) and (6) respectively.

(2004). Thus, we define a 15-neighbourhood, in which thirteen voxels are past voxels and two voxels are to be decided, as shown in Figure 2b,

$$\mathcal{N}_{15}(ijk;i,j+1,k)=\begin{bmatrix} (i-2,j,k-1) & (i-2,j+1,k-1) & (i-1,j,k-1) \\ (i-1,j+1,k-1) & (i,j-1,k-1) & (i,j,k-1) \\ (i,j+1,k-1) & (i-2,j,k) & (i-2,j+1,k) \\ (i-1,j-1,k) & (i-1,j,k) & (i-1,j+1,k) \\ (i,j-1,k) & & \end{bmatrix} \tag{6}$$

which will be used in our new three-directional MCMC scanning algorithm. The 15-neighbourhood is a direct extension of the 6-neighbourhood in 2D (Wu *et al.*, 2004). Details of the scanning algorithm using $\mathcal{N}_{15}$ follow in Section 2.3.

Thus, for V_{LMN} the rows, columns and layers of the MMRF form a stationary vector Markov chain of dimensions $(M+1)(N+1)$, $(N+1)(L+1)$ and $(L+1)(M+1)$, respectively, while the total number of voxels is $N_v=(M+1)(N+1)(L+1)$. For a h-order model with N_s states and $\mathcal{N}(h)$ neighbours, the computational complexity is $O\left(N_v \sum_{i=1}^{h} N_s^{\mathcal{N}(h)}\right)$ (Qian and Titerington, 1991b).

We can see that the computational intensity increases exponentially with the number of neighbours considered. For a binary porous medium (the situation addressed in this paper), $N_s=2$: pore and solid.

2.3. 3D SCANNING ALGORITHM

For the proposed MMRF model (6), estimating the parameters in the joint probability function (3) is very difficult. The problem is that the spatial association intrinsic to MRF models leads to a situation where the application of standard statistical approaches, such as maximum likelihood estimation, are computationally prohibitive. In fact, in most applications where standard maximum likelihood estimation is problematic, so too is the task

of producing a random sample, let alone developing them in three-dimensional contexts (Besag, 2000).

To overcome these difficulties, the standard approaches are replaced by MCMC simulations. To accomplish this, we have to construct a 3D Markov chain with state space X, which is straightforward to simulate and whose equilibrium distribution is $p(x)$. The chain is run for a sufficiently long time – i.e. sufficient size in the present discrete spatial context – so that the simulated structure of the chain reproduces the important statistical features of $p(x)$ for the real material. In effect, we construct a so-called ergodic Markov transition probability matrix. Wu *et al.* (2004) explored this approach in 2D and here we extend it to 3D.

As stated before, if 3D images were available, the neighbourhood structure (6) could be used directly to construct the 3D chain. However, in the absence of 3D information we describe below how to construct the 3D chain based on three perpendicular, independent, 2D images. For each 2D image a transition matrix is built using the 6-neighbourhood scheme described by Wu *et al.* (2004). In this 2D scheme the conditional probabilities for the sites (i, j) and $(i, j+1)$ are determined simultaneously, using a 5-neighbourhood $\mathcal{N}_5(ij)$ for (i, j) and a 6-neighbourhood $\mathcal{N}_6(i, j+1)$ for $(i, j+1)$, as shown in Figure 3. The chain in which this 2D scheme is used to scan the 2D image, is also part of the chain for the 3D model (step (ii)) described below. Wu *et al.* (2004) showed that in 2D this 6-neighbourhood was sufficiently large and they also found that the dual-site updating scheme was more efficient (faster) and more effective (better quality) than a mono-site updating scheme. To deal with the boundaries of the image, additionally the conditional probabilities for 1D 2- and 3-neighbourhoods and 2D 3- and 4-neighbourhoods are determined. For example, the 3- and 4-neighbourhoods are the reduced version of the 5- and 6-neighbourhoods shown in Figure 3 if $j = 1$, which are used as indicated in Figure 4b.

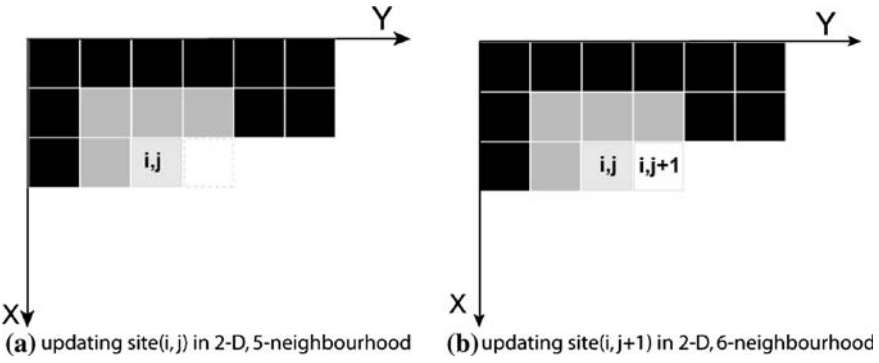

Figure 3. 5- and 6-neighbourhoods (in grey shades) used in 2D.

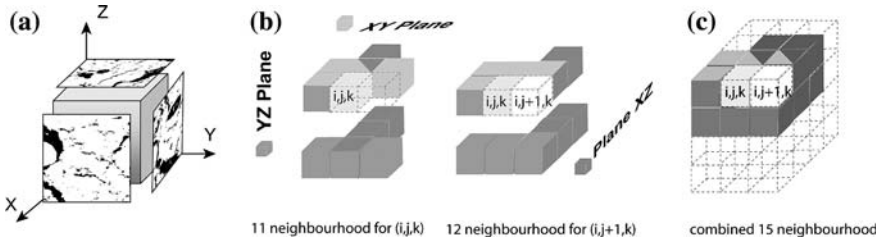

Figure 4. Illustration of combining 2D 5- and 6-neighbourhoods derived from (a) three perpendicular planes in 3D into (b) 11- and 12- neighbourhoods for updating the two voxels (i, j, k) and $(i, j+1, k)$ simultaneously, resulting into (c) the combined 15-neighbourhood. For example, the 11-neighbourhood combines a 5-neighbourhood in the XY plane (light grey), a 5-neighbourhood in the YZ plane (middle grey) and a 6-neighbourhood in the XZ-plane (dark grey). Note that two grey levels are marked for voxels from overlapping neighbourhoods, while (i, j, k) is part of all three neighbourhoods.

As in 2D, the 3D 15-neighbourhood shown in Figure 2b is built in 2 steps. First, a 11-neighbourhood $N_{11}(ijk)$ is constructed to determine the conditional probability for voxel (i, j, k) by combining the 2D 6-neighbourhood $\mathcal{N}_{j,6}(ijk)$ and the 5-neighbourhoods $\mathcal{N}_{i,5}(ijk)$ and $\mathcal{N}_{k,5}(ijk)$ shown in Figure 4b. To clarify the notation, for example $\mathcal{N}_{j,6}(ijk)$ denotes the 2D 6-neighbourhood of (i, j, k) in the plane with constant j, with associated conditional probability $p(x_{ijk}|x(\mathcal{N}_{j,6}(ijk)))$. Then, to determine the probability for $(i, j+1, k)$ the 6-neighbourhoods $\mathcal{N}_{i,6}(i, j+1, k)$, $\mathcal{N}_{j,6}(i, j+1, k)$ and $\mathcal{N}_{k,6}(i, j+1, k)$ are combined to form the 12-neighbourhood $\mathcal{N}_{12}(i, j+1, k)$ shown in Figure 4b. Notice, that the newly determined probability for voxel (i, j, k) is part of $\mathcal{N}_{i,6}(i, j+1, k)$ and $\mathcal{N}_{k,6}(i, j+1, k)$. Together, $\mathcal{N}_{11}(ijk)$ and $\mathcal{N}_{12}(i, j+1, k)$ form the 15-neighbourhood $\mathcal{N}_{15}(ijk; i, j+1, k)$ (6) shown in Figure 4c. Hence, this 15-neighbourhood is a direct generalisation of the previously developed 2D 6-neighbourhood.

The associated 3D transition probabilities $p(x_{ijk}|x(\mathcal{N}_{11}(ijk)))$ and $p(x_{i,j+1,k}|x(\mathcal{N}_{12}(i, j+1, k)))$ are calculated as

$$p(x_{ijk}|x(\mathcal{N}_{11}(ijk))) = \alpha\{p(x_{ijk}|x(\mathcal{N}_{i,5}(ijk))) + p(x_{ijk}|x(\mathcal{N}_{j,6}(ijk))) + p(x_{ijk}|x(\mathcal{N}_{k,5}(ijk)))\} \quad (7)$$

$$p(x_{i,j+1,k}|x(\mathcal{N}_{12}(i, j+1, k))) = \alpha\{p(x_{i,j+1,k}|x(\mathcal{N}_{i,6}(i, j+1, k))) + p(x_{i,j+1,k}|x(\mathcal{N}_{j,6}(i, j+1, k))) + p(x_{i,j+1,k}|x(\mathcal{N}_{k,5}(i, j+1, k)))\} \quad (8)$$

The averaging parameter α is determined based on matching the measured and the calculated porosities, as explained below.

To deal with different boundaries reduced 7-, 8-, 10- and 11-neighbourhoods are used instead of the 11- and 12-neighbourhoods. For example, 11- and 12-neighbourhoods in Figure 4b reduce to 7- and 8-neighbourhoods if $i=2$, $j=1$ as used in Figure 5c, based on 5- rather than 6-neighbourhoods in the planes with constant j. Expressions similar to (7) and (8) are used to calculate the transition probabilities for the reduced neighbourhoods.

Using the above neighbourhood scheme, the Markov chain is simulated as follows:

(i) At the beginning of the chain, the probability that the first voxel is pore is taken as the value of the porosity. Then, the first row is constructed in a 1D simulation (Figure 5a). using a 3-neighbourhood, for which the conditional probabilities are derived from the horizontal thin section (constant k).

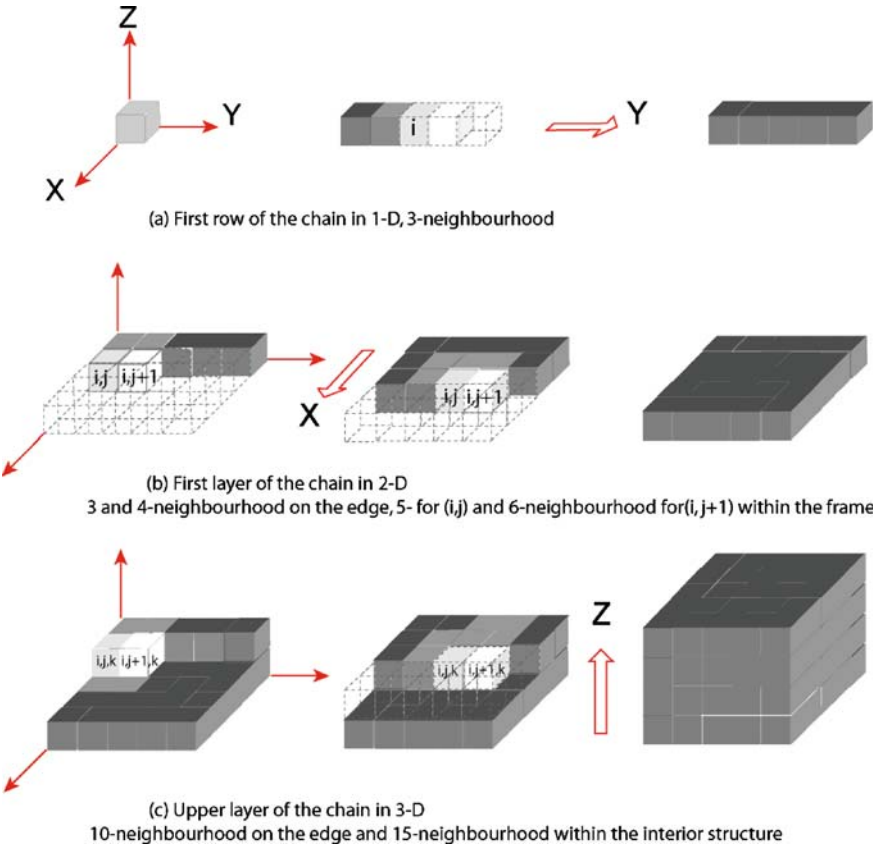

Figure 5. 3D chain construction illustration chart.

(ii) The second row is started with a 4-neighbourhood, also derived from the horizontal section (Figure 5b). Then, in one scan, we create row by row the first layer in a 2D simulation described by Wu *et al.* (2004), using the 6-neighbourhood with probabilities derived from the horizontal thin section.

(iii) The first row of the second layer is formed similar to the second row of the first layer (see step ii above), but now using a vertical 4-neighbourhood (constant i), followed by 6-neighbourhoods in the same plane. The second row of the second layer starts with reduced 7- and 8-neighbourhoods (Figure 5c) and continues with the reduced 10- and 11-neighbourhoods described above. Then, the inside rows and columns are built using the full 3D 15-neighbourhood described above.

To build the chain 2- and 3-neighbourhoods in 1D are determined, yielding 2^2 and 2^3 transition possibilities in the binary systems. Similarly, 3- and 4-neighbourhoods in two 2D sections are determined, accounting for 2×2^3 and 2×2^4 possibilities, while 5- and 6-neighbourhoods in all three 2D sections add up to 3×2^5 and 3×2^6 possibilities. Hence, a total of 348 conditional probabilities need to be determined.

For the present binary system, to determine the averaging parameter α in equations (7) and (8) it is sufficient to consider the probabilities for x_{ijk} and $x_{i,j+1,k}$ equal to 0 (pore) only. Obviously, $\alpha = 1/3$ reflects pure arithmetic averaging, but we choose to optimise this parameter by matching the porosity (fraction of pore voxels). After a single scan with $\alpha = 1/3$, we normally find that the porosity ϕ_c calculated from the reconstruction is up to 10% lower than the measured porosity ϕ. Then, adjusting α by $d\alpha = 0.1\,(\phi_c - \phi)$ the scans are repeated until the difference between the measured and calculated porosities is less than 0.1%. This usually happens within 4 scans and a typical final α value is 0.339.

2.4. RECONSTRUCTIONS OF POROUS ROCKS

We have applied the 3D modelling approach to a wide range of rocks and soils, encompassing perhaps 100–150 different materials to date. Here we describe a few results for a variety of rocks, ranging from coarse sandstone to a very fine mudrock, for which the data are summarised in Table I, to illustrate the capability of the new modelling approach. The measured permeability of these materials ranges over more than six orders of magnitude. In some cases, only a single thin section was available, in which case we assumed that the image characteristics of this single section applied in all directions. Then, our 3D Markov random field models were used to reconstruct the rock structures in 3D. Because we are interested in the

Table I. Characteristics of reconstructions and simulated permeabilities

Sample	Type	Image size (mm^2) and pixel size (μm)	Porosity (%)	Measured permeability (mD)	Simulated permeability (mD)
1	Deformed rock	1.30×0.92 (1.0)	17.87	82.1	71.5
2	Deformed rock	1.30×0.92 (1.0)	28.02	1406	1078
3	Deformed rock	1.30×0.92 (1.0)	13.15	2.31	0.5
4	Deformed rock	1.50×1.00 (2.0)	14.33	NA	0.48
5	Deformed rock	1.50×1.00 (2.0)	8.54	NA	2.2
6	Undeformed sandstone	3.0×1.9 (4.0)	27.17	2500	2236
7	Mudrock	0.490×0.365 (0.6)	22.64	0.32	0.38
8	Mudrock	0.490×0.365 (0.6)	11.73	0.013	0.024
9	Sandstone with deformed bands	9.0×6.0 (12)	31.64	NA	2410 (top layer) 12 (sheer band)
10	Soil	10×10 (33)	15.5*	NA	NA

*Average of the 3 thin section porosities, as the total porosity was not available.

pore system, we have termed these reconstructions pore architecture models (PAMs).

To obtain the model parameters (transition probabilities), thin sections were digitally imaged and the results were stored as binary arrays depicting grains + cements (solids) and pore spaces. The images covered sample areas ranging in scale from millimetres to centimetres. Typically, the images comprise binary maps containing 550×550 pixels (e.g. a 1.65×1.65 cm image area has a resolution of 1 pixel $= 30\,\mu$m, while an image 0.05 cm across has a resolution of 1 pixel $= 0.1\,\mu$m).

The numerical implementation allows the user to specify the number of voxels to be generated. Tests show that the number of voxels for which the simulated 3D architecture becomes stationary (stable ratio of pores to solids) depends on the degree of heterogeneity. For example, reconstruction of a homogenous material, such as a typical sandstone, requires at least 100^3 voxels, corresponding to a cube with side 0.3 cm for an image with 30 μm pixels. In contrast, an inhomogeneous sample may require 200^3 voxels and even larger sizes are needed for highly heterogeneous deformed rocks. The PAM method is very fast, as it takes only a few minutes to reconstruct a cube on a common Pentium IV PC. Obviously, the image analysis and data preparation take longer.

In Figure 6 the reconstructions for the samples of Table I are presented. For each of these samples only one thin section was available and

we assumed that the sections were statistically the same in the remaining perpendicular directions, except for sample 9. Visually, the agreement between the sections and the PAMs is good. However, more detailed comparisons between the images and the reconstructions will be carried out in the Sections 2.5 and 3. In Figure 7 a reconstruction is shown of a fairly heterogeneous soil (sample 10 in Table I), for which three perpendicular thin sections of a single core were available. Comparison of the sections

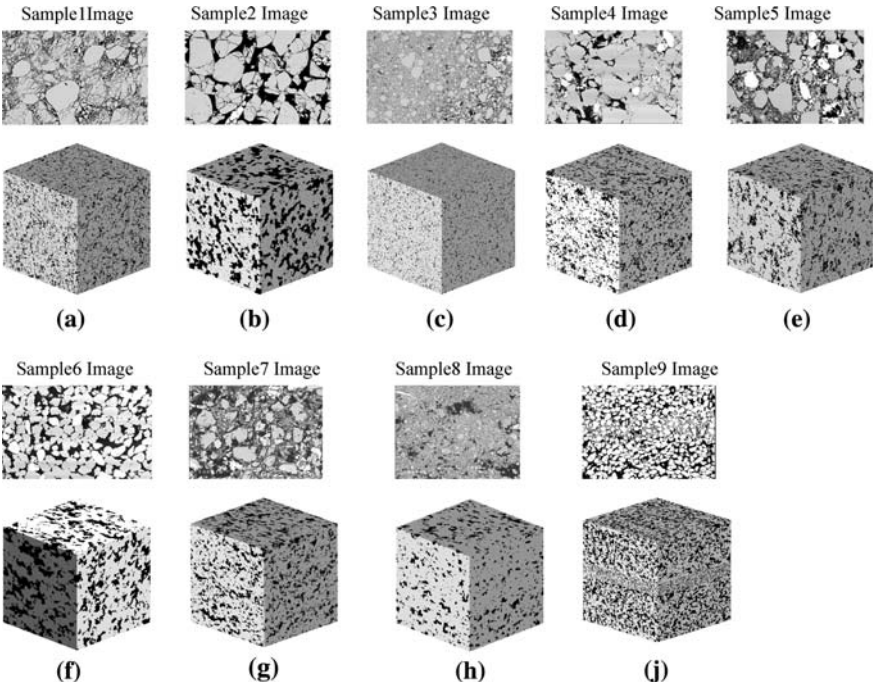

Figure 6. Simulations of various rocks with the corresponding thin sections, for samples 1 to 9 as detailed in Table I (black indicates pore space).

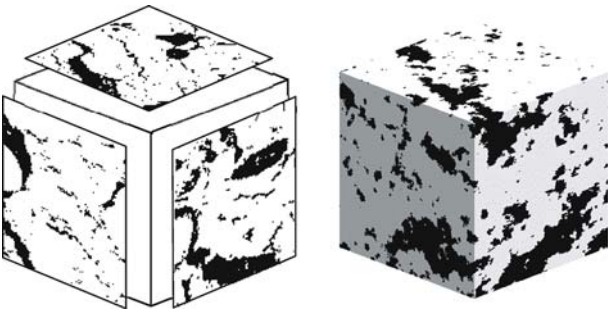

Figure 7. Simulation of a heterogeneous soil material based on three perpendicular thin sections (sample 10 in Table I).

and the PAM shows, for example, that the morphology and size of the void spaces have been qualitatively reproduced.

2.5. CALCULATION OF INTRINSIC PERMEABILITY

One of the least complicated macroscopic transport properties is the single-phase (intrinsic) permeability, which is estimated from a PAM using the Lattice–Boltzmann (LB) method. The advantage of LB is that non-equilibrium dynamics, especially those involving interfacial dynamics and complex boundaries (geometries), can be incorporated relatively easily (Kadanoff, 1986). In this paper we use the single-time relaxation scheme (Bhatnagar *et al.*, 1954), the so-called BGK model, with details as proposed by Qian *et al.* (1992) and Chen *et al.* (1991), in which the flow of a single-phase fluid is represented by a distribution of particles moving in a limited number of directions.

We use the 19-velocity model in 3D, i.e. D3Q19 where the particles move in 19 directions in the reconstructed 3D porous rock, which defines a three-dimensional grid of voxels, each of which maintains a nineteen particle distribution functions.

The pore-solid interface is assumed to be a non-slip boundary for water movement, where the water velocity is zero. One shortage of the BGK model is that the actual locations of the non-slip boundaries LB recovers varies with the relaxation time and, as a result, the simulated permeability is unrealistically a function of fluid viscosity (Li *et al.*, 2005). The multiple-relaxation scheme developed by Lallemand and Luo (2000) can overcome this problem but at the expense computational cost. As the aim of this work is to calculate the permeability of a single-phase flow, we simply use a relaxation time whose value is one to accurately locate the boundary. We define the 19 particle distribution functions at the centre of the each pore voxel so that the particle hits the water-solid boundary halfway in its one-time-step journey. All particles that hit the water-solid boundary halfway during their one-time-step journey are bounced back where they come from. Such treatment of the water-solid boundary is a special case of the scheme proposed by Filippova and Hanel (1998) for non-slip boundary and is second-order accurate. There are different ways to apply a driving force to fluid (Buick *et al.*, 2000), and in this work we used a pressure gradient in our simulations. The prescribed pressures are maintained the method proposed by Zou and He (1997). Details of treating the boundary and the calculation of the permeability from the LB simulation are given in Zhang *et al.* (2005).

Permeabilities of the reconstructions have been calculated using (typically) 200^3 voxels, which are equivalent to volumes of a few cubic millimeters to one cubic centimeter in the presented examples. The calculated

permeability values are compared with measured values in Table I, showing good agreement. This is a first indication that the PAM reconstruction approach is able to capture the characteristics of the pore system of the examined rocks.

3. Spatial Distribution of Pores and Pore System Topology

The success of PAMs in reproducing the measured permeabilities justifies further investigation of the reconstructed pore system. In this section we describe additional analyses that reveal details about the sizes of the pores and how they are connected, i.e. the geometrical and topological characteristics of the reconstructed medium. Unlike porosity, these characteristics of a porous medium control the transport properties. Currently, there is no universal standard to quantify these characteristics. Therefore, we introduce a new suite of methods called pore analysis tools (PATs), which are based on image analysis methods.

Within PATs, we identify each void space of the model using the PAMs as input. Using an iterative procedure, we fit into each void space a "structuring element" that consists of a pseudo-spherical aggregation of voxels, similar to Vogel and Roth (2001) and Silin *et al.* (2003). In this work we only use the "spherical" shape, although other shapes can be used too. Starting with the largest pore bodies, we fit the "equivalent" sphere into them. Then a smaller structuring element is fitted into the next smaller pores, etc, until the pore system is completely filled. We define the corresponding sphere diameter as the pore size.

The pore size distributions for three PAM realizations of one sample, sample 6 in Table I, are shown in Figure 8. The figure also shows the pores in the sample that are larger than 0.02 mm. The minimum pore size that can be determined is limited by the voxel size. To visualise the pore size distribution in the pore system, the pores have been depicted with different colours according to their sizes. For this example, the pore space is divided into 11 pore size classes ranging from 0.02 to 0.3 mm in diameter and the corresponding volume fraction of the pore space, i.e. the porosity, has been determined. The classes are determined by the sizes of the structuring elements. Using the pore size PAT, we illustrate the variation of pore size distributions from multiple PAM realisations in Figure 8. The close agreement of these curves demonstrates the stability of the PAM method.

Although there are no direct means of measuring pore size in the laboratory, the mercury injection porosimetry (MIP) method can be used to infer this characteristic (Matthews *et al.*, 1995). MIP is also helpful in investigating pore connectivity. MIP is based on capillary dominated liquid penetration into progressively smaller pores. Assuming cylindrical pores, the relationship between the applied mercury pressure P (psi), and the

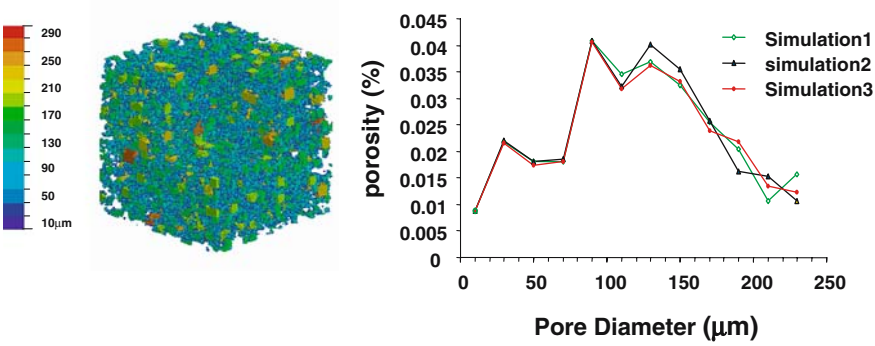

Figure 8. (a). Visualisation of pore size distribution and (b). corresponding curve for three realisations from sample 6 in Table I.

diameter D (m) of the corresponding pore being invaded, is expressed by the Young-Laplace equation

$$D = \frac{-4\gamma \cos\theta}{P} \tag{9}$$

The surface tension γ (dynes/cm^2) of mercury varies with purity, but the usually accepted value is 484 dynes/cm. The contact angle θ between the mercury and the solid, measured through the mercury, varies somewhat with solid composition, but is normally close to 130°.

In a mercury injection experiment the volume of the intruded mercury increases rapidly around a certain pressure, which depends on the pore size distribution. This is the percolation threshold pressure, which corresponds to an inflection point on the mercury injection curve, i.e. the graph of mercury pressure versus saturation. At this threshold pressure, the mercury forms an interconnected pathway throughout the sample (Katz and Thompson, 1986).

Since we know the pore size spatial distribution and how the pores are connected, it is straightforward to simulate a mercury injection process. Instead of replicating the usual (omni-directional) laboratory injection procedure, we simulate single-directional mercury injection through one of the six faces of the simulated cube. Figure 9 shows the simulated mercury injection curve for the reconstructed sandstone cube of sample 6, compared to the experimental curve. The two curves agree very well, suggesting that the PAM also reproduces critical details related to the connectivity of the pore system.

The pore connectivity is recognised as a key control on the flow properties of a medium. A topological parameter, to quantify the connectivity, is

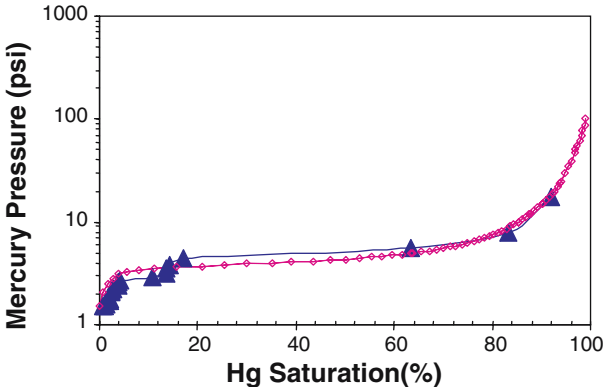

Figure 9. Simulated mercury injection curve (line with triangles) compared with experimental data (dotted line with circles) for sample 6.

the specific Euler number χ_V, which is defined by (Vogel, 1997; Vogel and Roth, 2001)

$$\chi_V = \frac{N - C + H}{V} \tag{10}$$

Equation (10) applies to a specific volume V of porous medium, with N isolated objects, C interconnected regions or loops (often referred to as the connectivity or genus), and H completely enclosed cavities (solid floating in void). Broadly speaking, a negative χ_V corresponds to high pore connectivity. Following Vogel (1997) we define a connectivity function, in which χ_V is calculated based on pore sizes ranging from a specified value up to the maximum pore size. This connectivity function is presented in Figure 10 for the realization of sample 6. Obviously for the small pore sizes, the connectivity is high as the pore size range on which χ_V is based, comprises almost all pores. However, there is a rapid increase in the specific Euler number between pore sizes 50 and 60 μm, indicating that the set of pores with sizes larger than these values are not interconnected. According to the MIP data for this sample (Figure 9), the percolation threshold pressure lies between 5.47 and 7.74 psi, which correspond, based on equation (9), to pore sizes of 45 and 50 μm, respectively. Thus the connectivity curve confirms the interpretation drawn from the mercury injection curve. This implies that the specific Euler number is a very useful topological parameter.

4. Discussion

The methods described in this paper represent a significant contribution to the tools that are available to understand the characteristics of porous rocks or soils. The PAM method provides reconstructions, which only

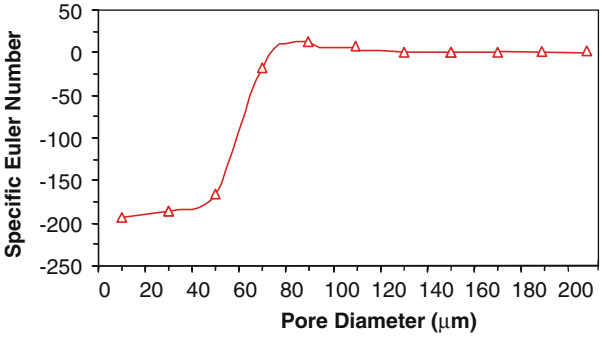

Figure 10. Connectivity function curve for sample 6, showing the specific Euler number, calculated for pore diameters ranging from the indicated size up to the maximum size.

require thin section images (or other image types, such as SEM scans) as input and is therefore essentially non-destructive. The PAMs can then serve as input to a variety of simulation and analysis tools (PATs). We have described some of those tools, which enable calculation of key flow properties of the porous material. The good correspondence between the calculated and measured flow properties – which does not require "tuning" or calibration – serves as an initial validation of the PAM method itself.

It may be clear that prediction of the flow characteristics requires more than determining the porosity and the pore size distribution. The pore connectivity, i.e. the topology of the pore system, must also be obtained to make robust predictions. Previous efforts to develop a representation of pore system topology have been based on extrapolation of 2D patterns inferred from thin section analysis (Okabe and Blunt, 2004) or have been directly determined from analysis of computerised tomography images (Lindquist *et al.*, 2000; Arns *et al.*, 2004). Based on additional work that we will publish separately, we believe that tomography techniques fail to capture important pore system connections that occur at the smaller pore sizes. We do not yet have a direct comparison to enable us to draw a firm conclusion, but we suspect that a thin section scheme only will create a good representation of the complex topology associated with the smaller pores.

In contrast, PAMs seem to capture at least part of the topology of real pore networks and with their geometric characteristrics (e.g. pore size distribution and spatial pattern of pores). This inference is based on the correspondence between mercury injection characteristics, and the shape of the connectivity function involving the specific Euler number, particularly the indication about the percolation threshold pore size. We are tempted to speculate that topological measures (which are amongst the characteristics

that can be determined using PATs) may enable us to make better predictions about the flow characteristics than we can obtain by laboratory methods – especially if we are interested in multi-phase flow properties.

5. Conclusions

The developments reported in this paper provide additional techniques, i.e. pore architecture models (PAM) and pore analysis tools (PAT), for investigating the characteristics of porous media. Additional work is required to determine if PAMs and PATs represent a significant advance over other methods. At this stage of the research, we can draw the following specific conclusions:

1. The PAM approach is an effective method to reconstruct (possibly heterogeneous) porous media. It seems applicable to a range of rock types, such as clean sandstones, deformed rocks, mudrocks and soils. An appealing aspect of this method is that it is fast and can be applied using information derived from thin sections or other readily obtained images.
2. Calculated single-phase (intrinsic) permeabilities of the reconstructed media, using the Lattice–Boltzmann method, closely match the corresponding laboratory values for a range of materials.
3. Both pore geometry (size) and topology (connectivity) are important for predicting the flow properties of a porous medium. Using a sphere-fitting method, we have determined the pore size distribution from a PAM. For the pore system derived from the PAM, we have simulated the mercury injection curve, which closely agrees with the experimental data.
4. A topological measure, the specific Euler number, indicates the size range of the set of interconnected pores. The smallest size in this range is the same as that inferred from mercury-injection data and corresponds to the percolation threshold. This indicates that topological characteristics are useful for predicting flow properties.

References

Adler, P. M., Jacquin, C. G., Quiblier, J. A.: 1990. Flow in simulated porous media, *Int. J. Multiphase Flow* **16**, 691–712.

Adler, P. M.: 1992, *Porous Media: Geometry and Transports*, Butterworth/Heineman, Stoneham.

Arns, C. H., Knackstedta, M. A., Pinczewskib, W. V. and Martys, N. S.: 2004, Virtual permeametry on microtomographic images, *J. Petrol. Sci. Eng.* **45**, 41–46.

Ball, B. C.: 1981, Modeling of soil pores as tubes using gas permeabilities, gas diffusivities, and water release, *J. Soil Sci.* **32**, 465–481.

Bakke, S. and Øren, P. E.: 1997, 3D pore-scale modeling of sandstone and flow simulations in pore networks, *SPE J.* **2**, 136.

Berryman, J. G. and Wang, H. F.: 2000, Elastic wave propagation and attenuation in a double-porosity dual-permeability medium, *Int. J. Rock Mech. and Mining Sci.* **37**, 67–78.

Besag, J.: 2000, Markov chain Monte Carlo for statistical inference. Center for Statistics and the Social Sciences, University of Washington, Working Paper No. 9.

Bhatnagar, P., Gross, E. P. and Krook, M. K.: 1954, A model for collision processes in gases: I. Small amplitude processes in charged and neutral one-component system, *Phys. Rev.* **94**, 511–525.

Biswal, B., Manwarth, C. and Hilfer, R.: 1998, Three-dimensional local porosity analysis of porous media, *Physica. A* **255**, 221–241.

Biswal, B., Manwart, C., Hilfer, R., Bakke, S. and Øren, P.E.: 1999, Quantitative analysis of experimental and synthetic microstructure for sedimentary rock, *Physica A* **273**, 452–475.

Blunt, M., Zhou, D. and Fenwick, D.: 1995, Three-phase flow and gravity drainage in porous media, *Trans. Porous Media* **20**, 77–103.

Buick, J. M. and Greated, C. A.: 2000, Gravity in a lattice Boltzmann model, *Phys. Rev. E* **61**, 5307–5320.

Chen, S., Chen, H. D., Martinez, D. and Matthaeus, W.: 1991, Lattice–Boltzmann model for simulation of magnetohydrodynamics, *Phys Rev. Lett.* **67**, 3776–3779; **32**, 1327–1354.

Coker, D. A., Torquato, S. and Dunsmoir, J. H.: 1996, Morphology and physical properties of Fontainebleau sandstone via tomographic analysis, *J. Geophys. Res.* **101**, 497–506.

Coles, M. E., Spanne, P., Muegge, E. L. and Jones, K. W.: 1994, Computer microtomography of reservoir core samples, *Proceedings of the 1994 Annual SCA Meeting*, Stavanger, Norway, September 12–14.

Coles, M. E., Hazlett, R. D., Muegge, E. L., Jones, K. W., Andrews, B., Siddons, P., Peskin, A. and Soll, W. E.: 1996, Developments in synchroton X-ray microtomography with applications to flow in porous media, paper SPE 36531, *Proceedings of the 1996 SPE Annual Technical Conference and Exhibition*, Denver, October 6–9.

Crawford, J. W., Matsui, N. and Young, I. M.: 1995, The relation between the moisture-release curve and the structure of soil, *Euro J. Soil Sci.* **46**, 369–375.

Currie, J. A.: 1961, Gaseous diffusion in porous media. 3: Wet granular materials, *Brit. J. Appl. Phys*. **12**, 275–281.

Dullien, F. A. L.: 1992, *Porous Media: Fluid Transport and Pore Structure*, 2nd edn. Academic Press, New York.

Dunsmoir, J. H., Ferguson, S. R., D'Amico, K. L. and Stokes, J. P.: 1991, X-ray microtomography: a new tool for the characterization of porous media, *Proceedings of the 1991 SPE Annual Technical Conference and Exhibition*, Dallas, October 6–9.

Fatt, I.: 1956, The network model of porous media: I, Capillary pressure characteristics, *Trans. AIME* **207**, 114.

Filippova, O. and Hanel, D.: 1998, Grid refinement for lattice-BGK models, *J. Comput. Phys*. **147**, 219–228.

Geman, S. and Geman, D.: 1984, Stochastic relaxation, Gibbs distributions, and the Bayesian restoration of images, *IEEE Trans. Pattn. Anal. Mach. Intell.* **PAMI-6**, 721–741.

Hazlett, R. D.: 1995, Simulation of capillary dominated displacements in microtomographic images of reservoir rocks, *Trans. Porous Media* **20**, 21–35.

Hazlett, R. D.: 1997, Statistical characterization and stochastic modeling of pore networks in relation to fluid flow, *Math. Geol.* **29**, 801–822.

Hilfer, R.: 2000, Local porosity theory and stochastic reconstruction for porous media, in: K. Mecke and D. Stoyan (eds.), *Statistical Physics and Spatial Statistics, Lecture Notes in Physics*, Vol. **254**, Berlin. Springer, 203 pp.

Joshi, M.: 1974, A class of stochastic models for porous media, PhD thesis, University of Kansas.

Kantzas, A., Chatziz, I. and Dullien, F. A. L.: 1988, Enhanced oil recovery by inert gas injection, paper SPE 13264, *Proceedings of the Sixth SPE/DOE Symposium on Enhanced Oil Recovery*, Tulsa, USA.

Kadanoff, L.: 1986, On two levels, *Phys. Today*, **39**, 7–9.

Katz, A. J., and Thompson, A. H.: 1986, Quantitative prediction of permeability in porous rock, *Phys. Rev.* **B 34**, 8179–8181.

Keller, A. A., Blunt, M. and Roberts, P. V.: 1997, Micromodel observations of the role of oil layers in three-phase flow, *Transp. Porous Media* **26**, 277–297.

Laakkonen, K.: 2003, Method to model dryer fabrics in paper machine scale using small-scale simulations and porous media model, *Int. J. Heat Fluid Flow* **24**, 114–121.

Lallemand, P. and Luo, L. S.: 2000, Theory of the lattice Boltzmann method: Dispersion, dissipation, isotropy, Galilean invariance, and stability, *Phys. Rev. E* **61**, 6546–6562.

Lerdahl, T. R., Øren, P. E. and Bakke, S.: 2000, A predictive network model for three-phase flow in porous media, paper SPE 59311, *Proceedings of the SPE/DOE Symposium on Enhanced Oil Recovery*, Tulsa, April 3–5.

Li, H. N., Pan, C. X. and Miller, C. T.: 2005, Pore-scale investigation of viscous coupling effects for two-phase flow in porous media, *Phys. Rev. E* **72**, Art. No. 026705 Part 2.

Liang, Z, Ioannidis, M. A. and Chatzis, I.: 2000, Geometric and topological analysis of three-dimensional porous media: pore space partitioning based on morphological skeletonization, *J. Colloid Interface Sci.* **221**, 13–24.

Lindquist, W. B., Venkatarangan, A., Dunsmuir, J. and Wong, T. F.: 2000, Pore and throat size distributions measured from synchrotron X-ray tomographic images of Fontainbleau sandstones, *J. Geophys. Res*. **105B**, 21508.

Mani, V. and Mohanty, K. K.: 1998, Pore-level network modelling of three-phase capillary pressure and relative permeability curves, *SPE Journal* **3**, 238–248.

Manswart, C. and Hilfer, R.: 1998, Reconstruction of random media using Monte Carlo methods, *Phys. Rev. E* **59**, 5596–5599.

Manswart, C., Torquato, S. and Hilfer, R.: 2000, Stochastic reconstruction of sandstones, *Phys. Rev. E* **62**, 893–899.

Marshall, T. J.: 1958, A relation between permeability and size distribution of pores, *J. Soil Sci*. **9**, 1–8.

Matthews, G. P., Moss, A. K. and Ridgway, C. J.: 1995, The effects of correlated networks on mercury intrusion simulations and permeabilities of sandstone and other porous-media, *Powder Technol.* **83**, 61–77.

McDougall, S. R. and Sorbie, K. S.: 1995, The impact of wettability on waterflooding: Pore-scale simulation, *SPE Reservoir Eng.* **August**, 208–213.

Müller, A. J. and Saez, A. E.: 1999, *The Rheology of Polymer Solutions in Porous Media, Flexible PolymerChains in Elongational Flow: Theories and Experiments*; Springer-Verlag, Heidelberg, pp. 335–393.

Okabe, H. and Blunt, J. M.: 2004, Prediction of permeability for porous media reconstructed using multiple-point statistics, *Phys. Rev. E* **70**, 066135.

Øren, P. E. and Pinczewski, W. V.: 1992, Mobilization of waterflood residual oil by gas injection for water wet systems, *SPE Form. Evaluat.* **7**, 70–78.

Øren, P. E., Billiotte, J. and Pinczewski, W. V.: 1994, Pore-scale network modelling of waterflood residual oil recovery by immiscible gas flooding, paper SPE 27814, *Proceedings of the Ninth SPE/DOE Symposium on Enhanced Oil Recovery*, Tulsa, April 17–20.

Øren, P. E., Bakke, S. and Arntzen, O. J.: 1998, Extending predictive capabilities to network models, *SPE J.* **3**, 324–336.

Øren, P. E. and Bakke, S.: 2002, Process based reconstruction of sandstones and predictions of transport properties, *Trans. Porous Media* **46**, 311–343.

Øren, P. E. and Bakke, S.: 2003, Reconstruction of Berea sandstone and pore-scale modelling of wettability effects, *J. Petrol. Sci. Eng.* **39**, 177–199.

Pereira, G. G., Pinczewski, W. V., Chan, D. Y. C., Paterson, L. and Øren, P. E.: 1996, Pore-scale network model for drainage dominated three-phase flow in porous media, *Trans. Porous Media* **24**, 167–201.

Qian, W. and Titterington, D. M.: 1991a, Multidimensional markov-chain models for image-textures, *J. Royal Stat. Soc. Ser.: B- Methodol.* **53**, 661–674.

Qian, W. and Titterington, D. M.: 1991b, Pixel labelling for three-dimensional sense based on markov mesh models, *Signal Process.* **22**, 313–328.

Qian, Y. H., Dhumieres, D. and Lallemand, P.: 1992, Lattice BGK models for Navier-Stokes equation, *Europhys. Lett*. **17**, 479–484.

Quiblier, J. A.: 1984, A new three-dimensional modelling technique for studying porous media, *J. Colloid Interface Sci.* **98**, 84–102.

Roberts, A. P.: 1997, Statistical reconstruction of three-dimensional porous media from two-dimensional images, *Phys. Rev. E* **56**, 3203–3212.

Silin, D. B., Jin. G. and Patzek, T. W.: 2003, Robust determination of the pore space morphology in sedimentary rocks, SPE 84296, in: *Proc. SPE Ann. Tech. Conf. and Exhib.*, Denver, October 2003.

Sorbie, K. S., Parker, A. and Clifford, P. J.: 1987, Experimental and theoretical study of polymer flow in porous media, *SPE Reservoir Eng.* **2**, 281–304.

Spanne, P., Thovert, J. F., Jacquin, C. J., Lindquist, W. B., Jones, K. W. and Adler, P. M.: 1994, Synchrotron computed microtomography of porous media: topology and transports, *Phys. Rev. Lett.* **73**, 2001–2004.

Spöler, C. and Klapp, S. H. L.: 2004, Vapor-liquid transitions of dipolar fluids in disordered porous media: Performance of angle-averaged potentials, *J. Chem. Phys.* **121**, 9623–9629.

van Dijke, M. I. J. and Sorbie, K. S.: 2002, Pore-scale network model for three-phase flow in mixed-wet porous media, *Phys. Rev. E* **66**, 046302.

van Dijke, M. I. J, Sorbie, K. S., Sohrabi, M., Danesh, A. and Tehrani, D.: 2004, Three-phase flow WAG processes in mixed-wet porous media: pore-scale network simulations and comparisons with water-wet micromodel experiments, *SPE J*. **9**, 57–66.

Vogel, H. J.: 1997, Morphological, determination of pore connectivity as a function of pore size using serial sections, *Eur. J. Soil Sci*. **48**, 365–377.

Vogel, H. J. and Roth, K.: 2001, Quantitative morphology and network representation of soil pore structure, *Adv. Water Resour.* **24**, 233–242.

Wanner, O., Cunningham, A. B. and Lundman, R.: 1995, Modelling biofilm accumulation and mass transport in a porous medium under high substrate loading, *Biotechnol. Bioengrg*. **47**, 703–712.

Wu, K., Nunan, N., Ritz, K., Young, I. and Crawford, J.: 2004, An efficient Markov chain model for the simulation of heterogeneous soil structure, *Soil Sci. Soc. Am. J.* **68**, 346–351.

Yeong, C. L. Y. and Torquato, S.: 1998a, Reconstructing random media, *Phys. Rev. E* **57**, 495–506.

Yeong, C. L. Y. and Torquato, S.: 1998b, Reconstructing random media: II. Three-dimensional media from two-dimensional cuts, *Phys. Rev. E* **58**, 224–233.

Young, I. M., Crawford, J. W. and Rappoldt, C.: 2001, New methods and models for characterising structural heterogeneity of soil, *Soil Till. Res.* **61**, 1–13.

Zhang, X. X., Bengough, A. G., Crawford, J. W. and Young, I. M.: 2002, A lattice BGK model for advection and anisotropic dispersion equation, *Adv. Water Res*. **25,** 1–8.

Zhang, X. X., Deeks, L. K., Bengough, A. G., Crawford, J. W. and Young, I. M.: 2005, Determination of soil hydraulic conductivity with the lattice Boltzmann method and soil thin-section technique, *J. Hydrol.* 306, 59–70.

Zou, Q. and He, X.: 1997, On pressure and velocity boundary conditions for the lattice Boltzmann BGK model, *Phys. Fluids.* **9**, 1591–1598.